

Health Monitoring of Rehabilitated Concrete Bridges Using Distributed Optical Fiber Sensing

Wei Zhang,* Junqi Gao, Bin Shi & Heliang Cui

Center for Engineering Monitoring with Opto-Electric Sensing, Nanjing University, Nanjing, China, 210093

&

Hong Zhu

College of Civil Engineering, Southeast University, Nanjing, China, 210096

Abstract: *It is evident that a health monitoring system (HMS) holds a great deal of potential to reduce the inspection and maintenance cost of existing highway bridges by identifying the structural deficiencies at an early stage, as well as verifying the efficacy of repair procedures. As newly developed techniques, distributed optical fiber sensing (DOFS) have gradually played a prominent role in structural health monitoring for the last decade. This article focuses on the employment of two types of DOFS, namely fiber Bragg grating (FBG) and Brillouin optical time domain reflectometry (BOTDR), into an integrated HMS for rehabilitated RC girder bridges by means of a series of static and dynamic loading tests to a simply supported RC T-beam strengthened by externally post-tensioned aramid fiber reinforced polymer (AFRP) tendons. Before the loading tests, a calibration test for FBG and another one for BOTDR were implemented to, respectively, obtain good linearity for both of them. Monitoring data were collected in real time during the process of external strengthening, static loading, and dynamic loading, respectively, all of which well identified the relevant structural state. The beam was finally vibrated for 2 million cycles and then loaded monotonously to failure. Based on the bending strength of externally prestressed members, ultimate values for the test specimen were numerically computed via a newly developed sim-*

plified model, which satisfactorily predicted the ultimate structural state of the beam. And then the alert values were adopted to compare with the monitoring results for safety alarm. The investigation results show a great deal of applicability for the integrated SHM by using both DOFS in rehabilitated concrete bridges strengthened by external prestressing.

1 INTRODUCTION

The inspection and maintenance work of existing highway bridges is now an urgent task most nations' infrastructure administrators must face. Because a higher quality inspection method can provide a more dependable assessment of bridges for the decision of maintenance strategy, it is evident that a health monitoring system (HMS), either real time or periodic, holds a great deal of potential to reduce the inspection and maintenance cost by identifying the structural deficiencies at an early stage, as well as verifying the efficacy of repair procedures (Aktan, 2000).

As newly developed techniques, optical fiber sensing has gradually played a prominent role in structural health monitoring for the last decade due to its prominently high durability, large data transmission bandwidth, and inherent immunity to electric or electromagnetic interference (Ansari, 1997). In particular,

*To whom correspondence should be addressed. E-mail: wzhang@nju.edu.cn.

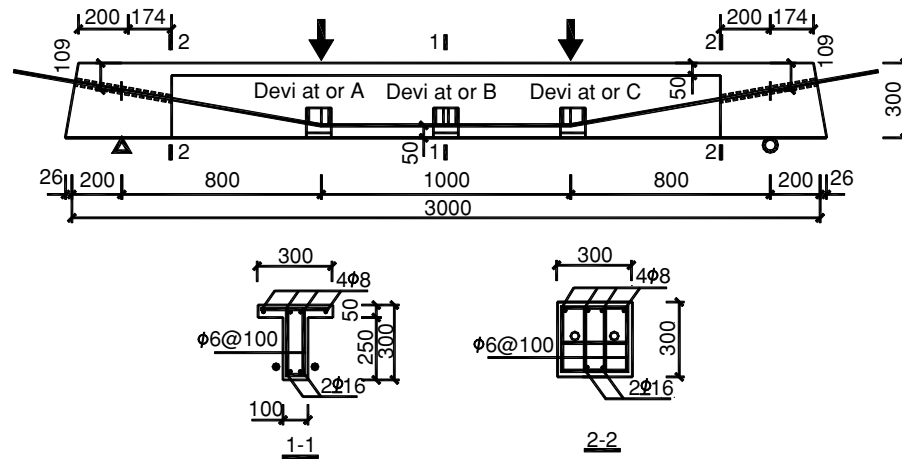


Fig. 1. General profile of the T-beam and its sectional reinforcement.

distributed optical fiber sensing (DOFS) techniques such as fiber Bragg grating (FBG) (Maaskant, 1997; Davis, 1997; Casas, 2002; Lin, 2004) and Brillouin optical time domain reflectometry (BOTDR) (Bao, 2001; Kurashima, 1997; Hiroshige, 2001; Wu, 2003) are capable of multiplexing a good number of sensors on a single optical fiber, which allows for a reduction in the cost per measurement point. However, little work to date has concentrated on the deployment of both DOFS techniques into the health monitoring of highway bridges under rehabilitation.

With regard to the various strengthening methods for the rehabilitation of existing bridges, external prestressing is considered to be one of the most appropriate choices for a majority of bridges due to its easy implementing and checking without traffic interruption. Especially with the recent employment of composites such as carbon fiber reinforced polymer (CFRP) or aramid fiber reinforced polymer (AFRP) instead of steel as post-tensioned tendons, the immunity against corrosion, which is the chief deficiency of external prestressing using steel tendons, can be well provided. The study presented herein demonstrates the applicability of both FBG and BOTDR sensing to the HMS of rehabilitated RC girder bridges by means of a series of static and dynamic loading tests to a simply supported RC T-beam strengthened by externally post-tensioned AFRP tendons. In addition, the corresponding numerical example of the test specimen was employed to identify the alert values of the HMS for a structural state evaluation.

2 DESCRIPTION OF SPECIMEN AND STRENGTHENING METHOD

The test specimen S1 was a simply supported T-beam with rectangular sections on both ends for external post-

ensioned anchorage, and the surface of both ends were pre-casted inclined planes to fit the anchors perpendicularly. Figure 1 illustrates the general profile of the beam as well as the sectional reinforcement. Three deviators were deliberately mounted on the bottom of the beam to keep the externally post-tensioned tendons in a double-draped profile for the four-point bending load.

Two round PVC ducts, both with diameters of 40 mm, were obliquely reserved inside both rectangular parts on each vertical side of the beam, into which an AFRP composite tendon (DUPONT Chemical Co. Ltd., USA) will, respectively, get through for external post-tensioning, with a diameter of 11 mm and an area of 95 mm². A tensile stress up to 588 MPa is to be established inside each tendon through prestressing by using two tailor-made anchorage devices, with its anchoring mechanism attributing to the bonding effects of a kind of special resin inside the cavity of the anchors. Figure 2 shows one end of the AFRP tendon connected to its corresponding anchorage device.

General mechanical properties of the relevant material such as concrete, reinforcing bar, and AFRP tendon are listed in Table 1.

3 CONFIGURATION OF THE HMS

3.1 Layout of sensors

Because flexural failure is the major failure mode for simply supported beams, the sensors employed were primarily arranged to measure the compressive strains on the top surface of the beam, as well as the tensile strains along the tendons, so as to evaluate the flexural capacity of the test specimen.

Due to the fragile behavior of bare gratings, encapsulation is testified to be efficient for FBG sensors to survive the tough operating environment in civil engineering.

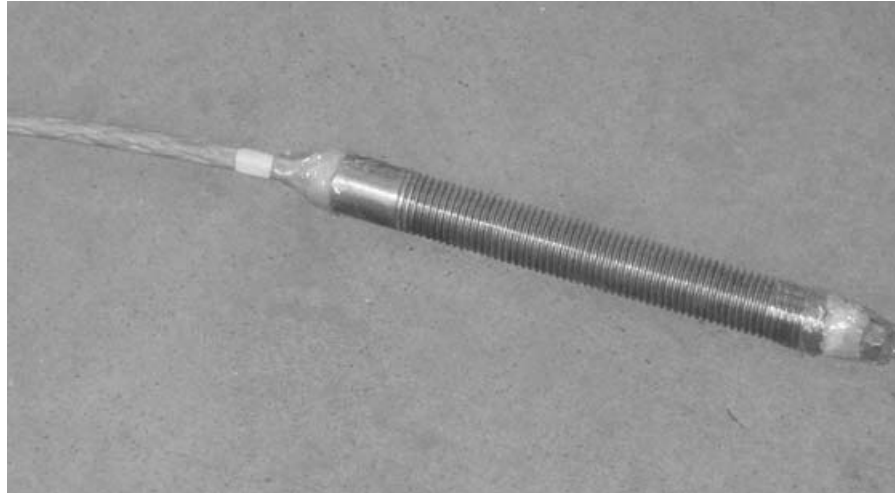


Fig. 2. AFRP tendon and its anchorage device.

Table 1
Mechanical properties of material

Concrete	
Modulus of elasticity (GPa)	32.3
Compressive strength (MPa)*	37.6
Steel bar	
Modulus of elasticity (GPa)	209
Tensile strength (MPa)	560
Yielding strength (MPa)	390
AFRP tendon	
Modulus of elasticity (GPa)	62.2
Nominal tensile strength (MPa)	1,200

*Cubic compressive strength.

Thus three slice-based encapsulated FBG sensors were mounted onto the top surface of one flange of the T-beam, with each connected end-to-end in an array, to acquire the static or dynamic strain of the specimen. The sensors had their nominal center wavelengths of 1,535, 1,545, and 1,553 nm, respectively, together with a gauge length of 80 mm, a measuring range of $\pm 2,500 \mu\epsilon$, a strain gauge factor of 1.2 pm/ $1 \mu\epsilon$ and a working temperature between -20°C and $+80^\circ\text{C}$. For the sake of verification and comparison, three electrical resistance strain (ERS) gauges were also mounted onto another flange, opposite to their relevant FBG sensors, respectively. The layout of the FBG sensors and ERS gauges is depicted in Figure 3a.

On the other hand, concerning BOTDR, overall bonding method (OBM) is performed with an optical fiber entirely bonded along one of the two AFRP tendons before pulling it through the reserved duct. Due to the round sectional profile of the tendon, fiber-optic sensors with such a long gauge is a sound choice for the measurement of the static distributed strains along the tendon.

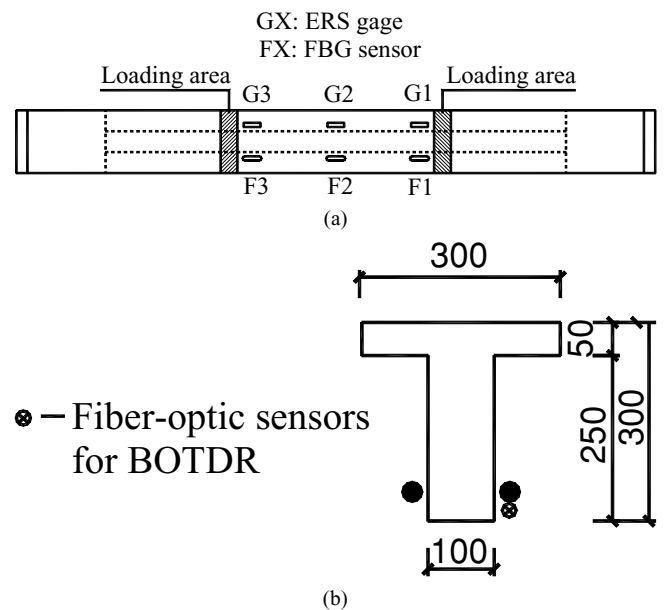


Fig. 3. Layout of sensors: (a) Layout of FBG sensors and ERS gauges; (b) Layout of fiber-optic sensors for BOTDR.

A certain type of jacketed SM optical fiber (Coning, Co. Ltd., USA) was chosen as the sensor, with a diameter of $900 \mu\text{m}$, a tensile strength of 5 GPa, a working temperature between -20°C and $+80^\circ\text{C}$ and a calibrated strain gauge factor of 500 MHz/ $100 \mu\epsilon$. The layout of the fiber-optic sensors for BOTDR is depicted in Figure 3b.

3.2 Temperature compensation

Measuring structural response in a form of strain or deflection is of most interest for a HMS, so considering the influence of temperature shift to either FBG or

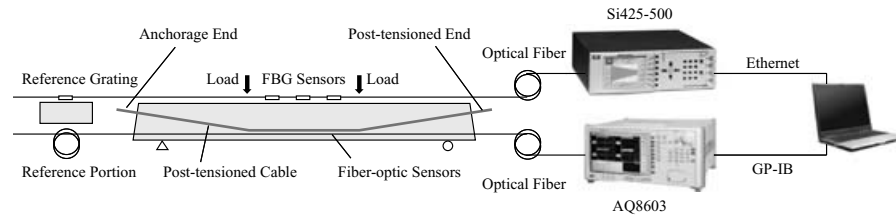


Fig. 4. Configuration of the HMS.

BOTDR, temperature compensation needs to be done to obtain the actual strain resulting from the deformation under the load. Therefore, with respect to FBG, a reference FBG sensor, with a nominal center wave length of 1,550 nm, was mounted on the top surface of an untouched concrete block made of the same material as the test specimen, and then the part of center wavelength shift caused by temperature shift can be directly read out and eliminated. On the other hand for BOTDR, a part of optical fiber, with a length of about 2 m, is bonded along an extra AFRP tendon kept in a state without any stress, and in light of the similar procedure as FBG, the part of frequency shift caused by temperature shift was to be excluded.

3.3 Configuration of HMS

A sound HMS requires an effective integration of various specialized diagnostic tools for operation (Aktan, 2000), and with regard to the distributed fiber-optic HMS herein, two distinct demodulators, or interrogators in other words, are integrated to cooperate for the demodulation of FBG and BOTDR, respectively.

On the one hand, a si425–500 optical sensing interrogator (Micron Optics, Inc., USA) was employed for the FBG sensors, with a maximum sampling frequency of 250 Hz, a resolution corresponding to $0.1 \mu\epsilon$, a repeatability corresponding to $0.24 \mu\epsilon$ and a dynamic range of 25 dB. Furthermore, the si425–500 communicated with the control terminal, a notebook computer, via an Ethernet cable for the transmission of the enormous monitoring data.

On the other hand, an AQ8603 optical fiber strain/loss analyzer (ANDO Electric, Co. Ltd, Japan) was employed meanwhile to measure the distributed strain of the jacketed SM sensing optic fiber along the AFRP tendon, with a minimal spatial resolution of 1 m, a measurement accuracy of $\pm 40 \mu\epsilon$, a strain measuring range of $\pm 15,000 \mu\epsilon$, a repeatability of 0.04% and a dynamic range of 4 dB. Being embedded in an industrial control computer, the AQ8603 can directly store the measuring data onto its hard disk and present the relevant strain values through a series of pre-installed software. Nev-

ertheless, the AQ8603 was still connected to the same notebook computer via a GP-IB cable for the convenience of a remote control.

Figure 4 depicts the general configuration of the HMS using distributed fiber-optic sensing.

4 CALIBRATION TEST RESULTS

Before the loading tests, a calibration test for FBG and another one for BOTDR were implemented to evaluate their respective behavior of linearity.

A slice-based encapsulated FBG sensor was attached next to an ERS gauge on a thick steel plate, and the plate was then fastened on a material test machine, subjected to a tensile or compressive load step by step. Figure 5 demonstrated the correlation between the center wavelength of the FBG sensor and the strain of the ERS gauge, and a good linear agreement, with a correlation coefficient of 0.999, can be well observed.

Concerning the distributed fiber-optic sensors for BOTDR, a jacketed SM optical fiber was bonded along an AFRP tendon, whereas two extensometers, with both gauge length of 250 mm, were attentively mounted onto the surface of the tendon by adhesive. The tendon was

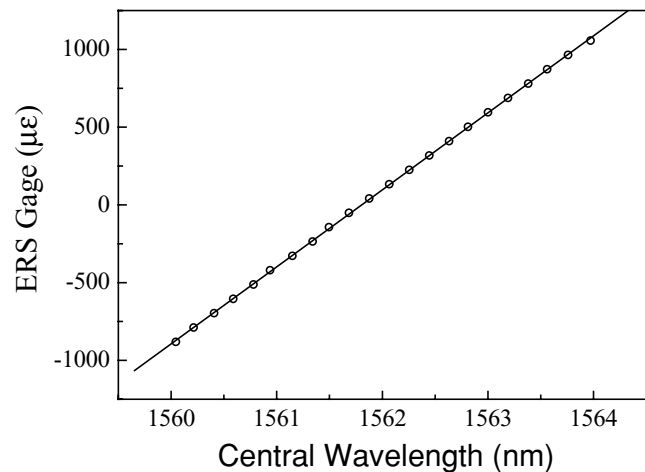


Fig. 5. Correlation between FBG sensor and ERS gauge.

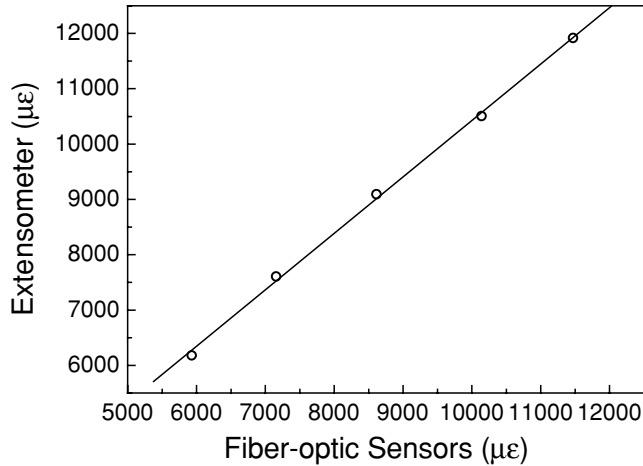


Fig. 6. Correlation between distributed fiber-optic sensor and extensometer.

then seated on a special pedestal for a step-by-step post-tensioning test. Figure 6 illustrates the correlation between the mean strain values obtained, respectively, from the fiber-optic sensors and the extensometers, and a good linearity, with a correlation coefficient of 0.999, can be well observed.

5 LOADING TEST PROCEDURES AND MONITORING RESULTS

5.1 Loading test procedures

The original test specimen was pre-loaded in the first place to simulate its damage process, and then the external strengthening was implemented for a rehabilitation of its load-carrying capacity. And then, the rehabilitated specimen was loaded both statically and dynamically for a validation of the efficacy of the strengthening, while

the structural state was monitored in real time by the established HMS. And finally, after 2 million cycles of oscillations, the specimen was loaded monotonously to failure.

Figure 7 shows the aspect of the rehabilitated specimen and the test apparatus. As can be seen the vertical load from an electro-hydraulic force servo system was applied to the test specimen via a simply supported distribution beam. In addition, two load cells, both mounted at the tensioned end, were employed to control the post-tensioned forces. And three extensometers, with their respective distance of 60, 125, and 200 mm to the bottom surface of the beam, were mounted in the mid-span of the beam to calculate the compression strain value on top of the beam surface based on Bernoulli's principle.

5.2 Monitoring results of pre-loading and reloading process

During the pre-loading process, the original T-beam S1 was loaded monotonously from 0 to 40 kN when cracks occurred at the bottom of the beam, and then unloaded to zero and externally strengthened by two post-tensioned AFRP tendons, both with a stress of about 588 MPa. And then it was reloaded monotonously to 100 kN.

Figure 8 indicates the comparison of recorded strains obtained from FBG sensor F1, ERS gauge G1, and the extensometers, in which the three traces of strain values show good agreement, but some diversities still remain among them. It is evident that cracking occurred after the load of 20 kN due to an obvious rigidity reduction, and an invert arch was formed after the post-tensioning with a tensile strain value of about $100 \mu\epsilon$ on top of the beam, and then the rehabilitated beam behaved in good linearity up to the load of 100 kN.

It is likely that the cracking of the concrete was responsible for the measuring diversities among the three

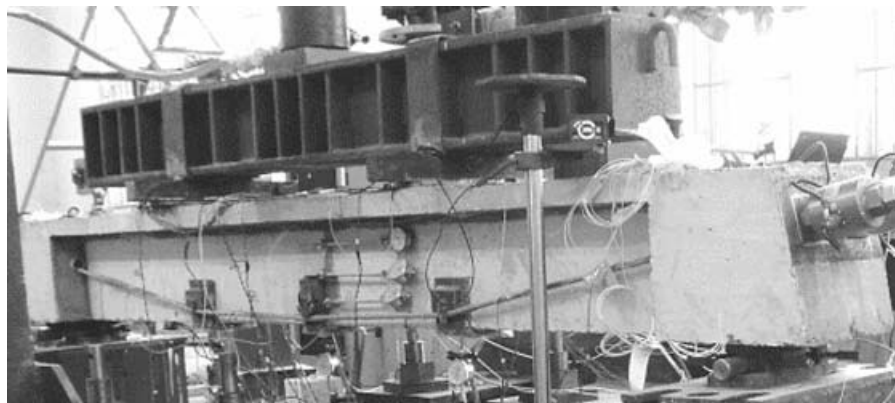


Fig. 7. Aspect of the rehabilitated specimen and the test apparatus.

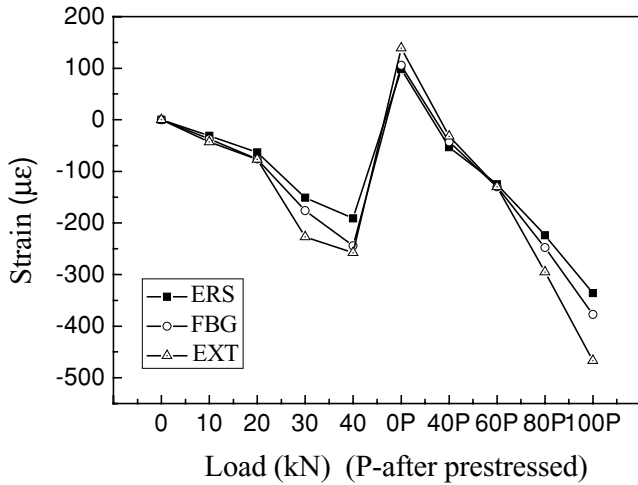


Fig. 8. Comparison of strains obtained from the three means.

methods because diversities only occurred after cracking. And the location of the gauges relative to the location of the cracks could cause local strain variations of the type observed.

Moreover, the trends of strains obtained from the other two FBG sensors and their relevant ERS gauges are very similar to the ones indicated in Figure 8.

Figure 9 illustrates the strain trend along the measured AFRP tendon. The fiber-optic sensors between the distributed distance of 626.95 and 627.95 m, with a length of 1 m between the two loading points, have similar strain values as one another under each load, while those between the distributed distance of 627.95 and 628.45, with a length of 0.5 m outside the deviating point, have continuously decreasing strain values, which may account for the prestressing loss when the tendon was passing

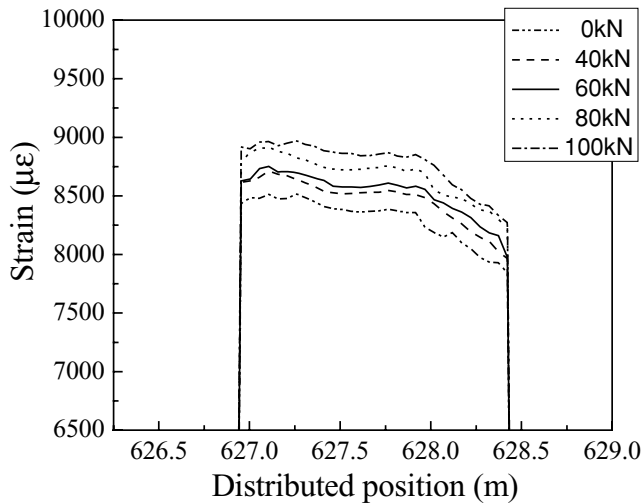


Fig. 9. Trend of distributed strains along the measured AFRP tendon.

by a deviator. In addition, a linear increase of the distributed strains along the measured tendon can also be well observed from 0 to 100 kN.

5.3 Monitoring results of static and dynamic loading test

After the reloading process, a dynamic load, ranging from 40 to 100 kN, was cyclically imposed on the rehabilitated beam to vibrate in a frequency of 5 Hz so as to simulate the operating state of rehabilitated concrete bridges. The dynamic load, respectively, paused on the vibration cycles of 20 thousand times, 50 thousand times, 100 thousand times, and 200 thousand times for a static loading test each, when the rehabilitated beam was loaded monotonously from 40 to 100 kN for an identification of its structural state.

Figure 10 illustrates the comparison of dynamic strains obtained from FBG sensor F1 during the process of vibration, including four sine waveforms within a period of 2 seconds, which are picked out, respectively, from the vibrating sine waveforms just before the pauses. As can be seen, an increase of the dynamic strain amplitudes, as well as a decrease of the absolute values of the dynamic strain under the minor load of 40 kN, occurred along with the increment of vibration cycles, which indicates a gradual rigidity attenuation resulting from cracking development inside the rehabilitated beam under oscillation.

Figure 11–14, respectively, illustrates the strain trends automatically collected by the HMS, together with the concrete strains collected manually from the ERS gauges and the extensometers. Because of close similarity, only the monitoring results from FBG sensor F1 and ERS gauge G1 are presented.

However, what has to be mentioned is that the strain gauges were all ruined successively because of vibration with infinite strain values by 200,000 cycles. Thus in

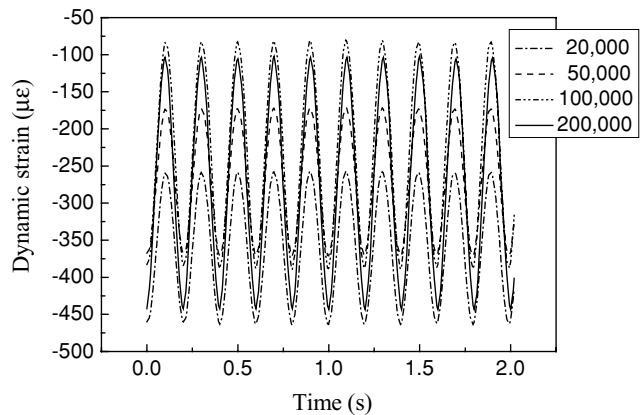


Fig. 10. Comparison of dynamic strains.

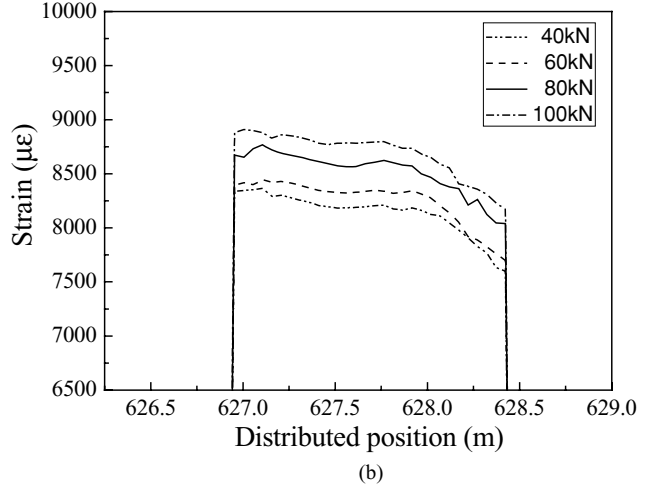
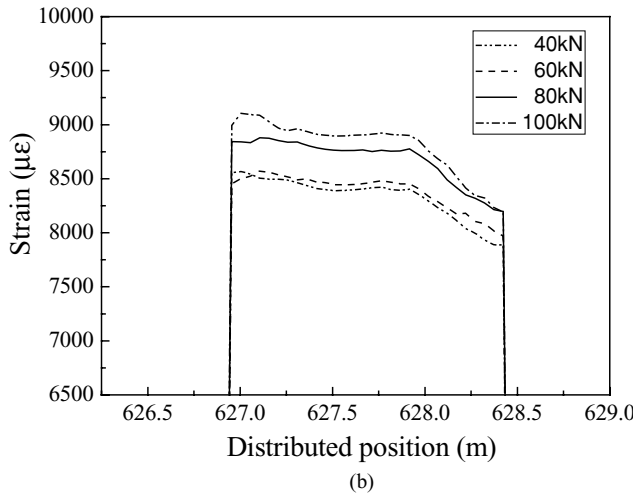
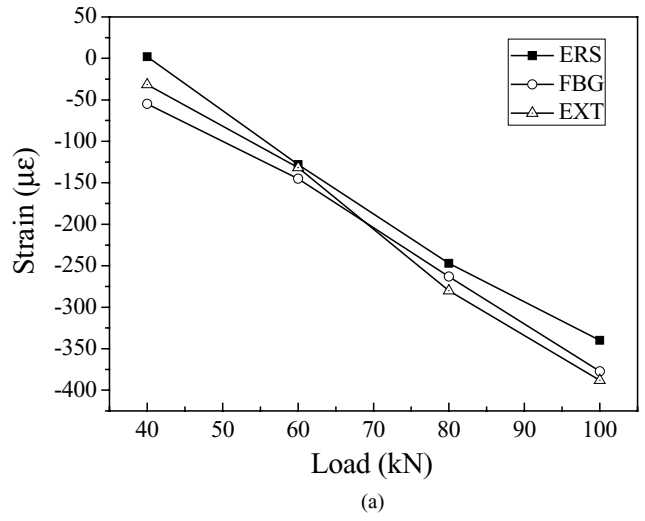
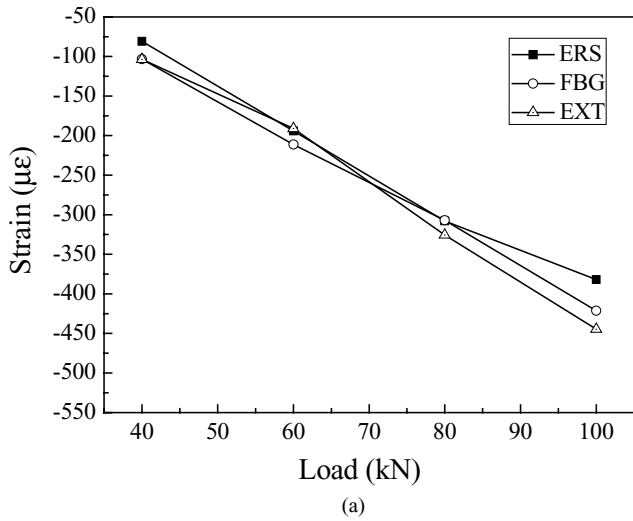


Fig. 11. Comparison of strains after 20,000 cycles: (a) Trend of concrete strain; (b) Trend of tendon strain.

Fig. 12. Comparison of strains after 50,000 cycles: (a) Trend of concrete strain; (b) Trend of tendon strain.

Figure 14a only the monitoring results from F1 and those from the extensometers are presented.

Good strain linearity of both concrete and tendon is shown in Figure 11–14. However, it can also be observed that the trend of strain response over time altered with oscillation cycles. For instance, with regard to concrete, the absolute strain values under 100 kN decreased after 50,000 cycles compared with those after 20,000 cycles, and then kept almost the same after 100,000 cycles, and finally increased after 200,000 cycles. Although for the tendon, the distributed strain values under 100 kN kept decreasing from 20,000 cycles to 200,000 cycles by and large.

The reason why strain values altered with oscillation cycles lies in the fact that the height of the compressive region of concrete decreased with cracking development under fatigue, which increased the arm of force to ten-

sons so as to decrease the horizontal resultant in light of the moment-equilibrium condition of the section. Thus the continuous strain decrease in tendons can be well explained. However, the strain of the upper-flange started increasing when the height of the compressive region was small enough to cause the strains in the compressive region to be almost uniform. Figure 15 illustrates the cracking conformation of the specimen S1 under the load of 100 kN after 200,000 cycles of oscillations. It can be observed that both bending cracks and shearing cracks occurred in the web.

5.4 Failure test results

The specimen S1 was finally vibrated for 2 million cycles without failure, and then loaded monotonously from 40 to 220 kN. Then the concrete in the upper flange started crushing while the tendons broke off abruptly

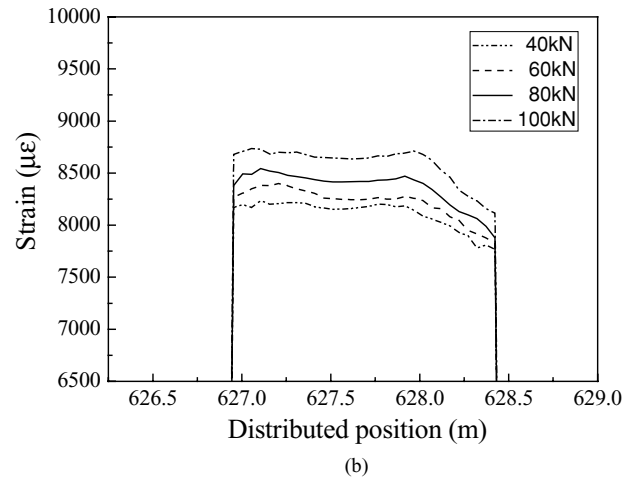
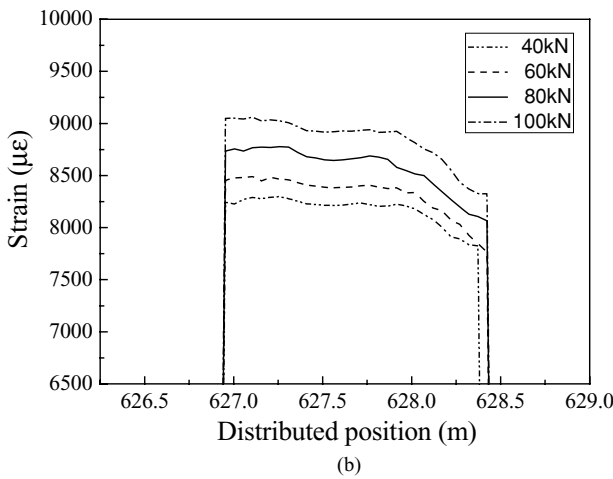
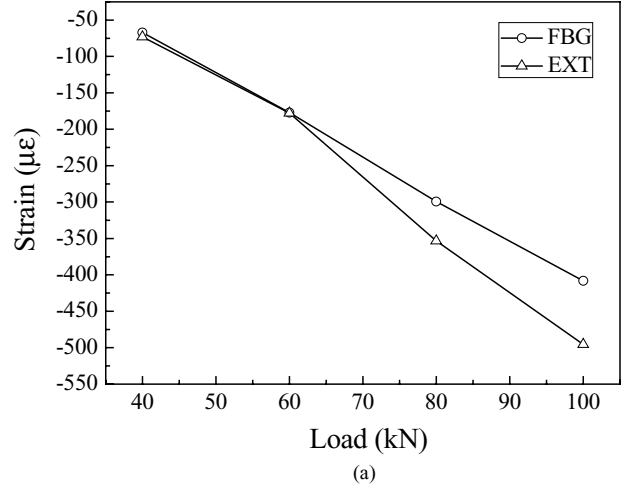
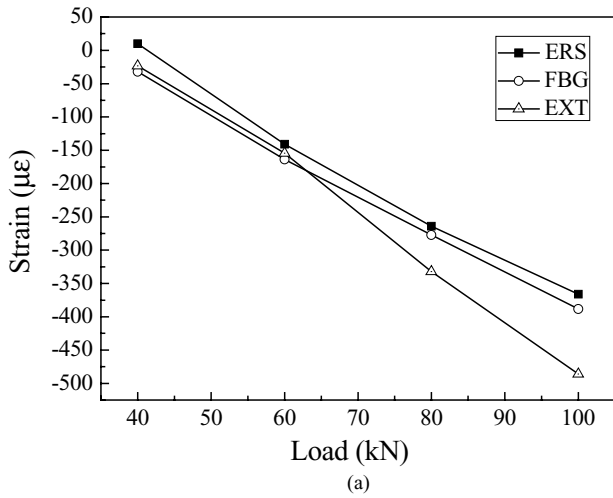


Fig. 13. Comparison of strains after 100,000 cycles: (a) Trend of concrete strain; (b) Trend of tendon strain.

Fig. 14. Comparison of strains after 200,000 cycles: (a) Trend of concrete strain; (b) Trend of tendon strain.

under the outer deviators to result in a load-carrying disability. Thus an ultimate bending strength of 88 kNm can be figured out. Figure 16 illustrates the cracking conformation of S1 on failure.

To consider the influence of fatigue to bending strength, another specimen S2 with the same dimension

and configuration was loaded monotonously to failure, when the load reached 220 kN and the concrete in the upper flange was crushed to result in a failure. Figure 17 illustrates the cracking conformation on failure. A close similarity can be well observed by comparing both cracking conformations in Figures 16 and 17.

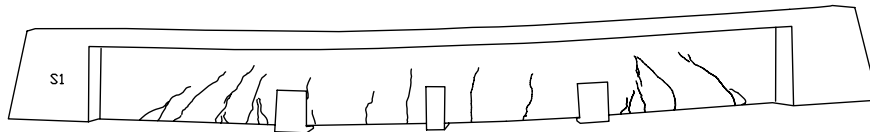


Fig. 15. Cracking conformation after 200,000 cycles.

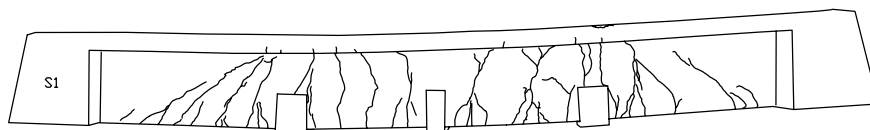


Fig. 16. Cracking conformation on failure.

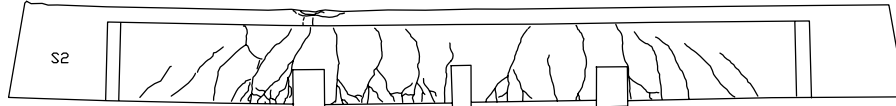


Fig. 17. Cracking conformation on failure of S2.

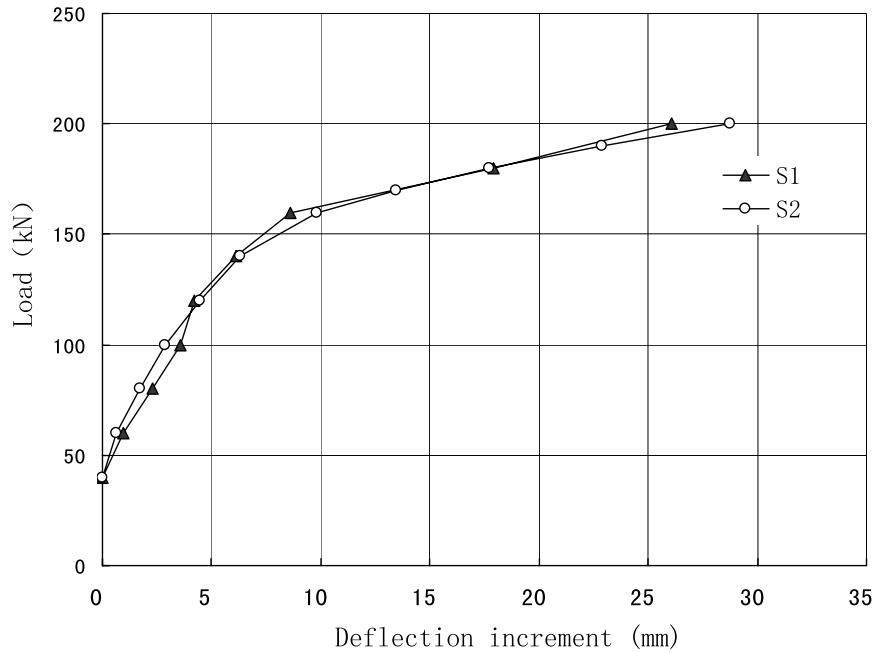


Fig. 18. Comparison of load-deflection increment curves.

Figure 18 shows the comparison of load-deflection increment curves of both test beams from the load of 40–200 kN, but not 220 kN due to the tendon abruption of S1. A close similarity also appears in Figure 18, only with the rigidity of S1 being a little less than that of S2 between the load of 40 and 100 kN, which is caused mainly by fatigue.

In fact, the strengthened T-beam in ultimate state can be considered as a tied-arch because of the existence of bending and shearing cracks in the web, with the upper-flange being the arch and the tendons being the tie bars. And thus the ultimate load is determined only by the compressive strength of concrete and the tensile strength of tendons. Because the fatigue load only aggravated the development of the cracks in the web but did not influence the strength of concrete or tendons, a primary conclusion can be drawn that the ultimate bending strength was not decreased even after 2 million cycles of oscillations in this test. In addition, the eruption of tendons of S1 is observed to be caused by the repeated rub between the tendons and the outer deviators, which weakened the area of tendons.

6 ESTABLISHMENT OF ALERT VALUES

With regard to a HMS for a bridge, one of the essential functions is to alert the appropriate officials in case of any reduction of the reliability of the bridge to an unacceptable level (Aktan, 1998). Thus, a series of alert values for the reliable performance of the bridge will be established by using various criteria. However, one of the most direct and simple approaches can be attributed to the ultimate state of the bridge structures, especially the bending failure state for rehabilitated girder bridges.

The provisions in the 2004 “AASHTO LRFD Bridge Design Specifications” have provided a procedure for the computation of nominal bending strength of reinforced, prestressed and partially prestressed concrete members, and in light of them the bending strength of a strengthened girder bridge using external prestressing can be generally identified (Naaman, 1995). However, the provisions do not have adequate applicability for the establishment of alert values because they do not take the influence from second-order effects into account (Tan, 1997), which always associates with an

overestimate of the bending strength of externally prestressed members, and the relevant overestimated alert values will ultimately result in an alarm disability to the rehabilitated girder bridges in an unreliable state.

In this section, a simplified model was developed for externally prestressed concrete beams with a view to second-order effects, so as to exactly compute the bending strength in a simple manner. Finally, the alert values of the test specimen were identified by the developed approach, and compared with the results stemming from the HMS.

6.1 Development of a simplified mechanical model

Generally speaking, second-order effects in externally prestressed members result from the fact that the external tendons are free to move relative to the axis of the beam between the anchorages or between the deviator points and anchorages, which leads to a gradual change in their eccentricity, with increasing member deformation giving rise to this influence (Harajili, 1999).

For the purpose of simplification, the nonlinear behavior of the members in an ultimate limit state was represented only by a plastic hinge with a certain distributed length. Figure 19 illustrates the actual distribution, together with the ideal distribution, of curvatures along a beam in its ultimate bending state, where a plastic hinge exists between a distance of $2Z_p$. Take advantage of the ideal curvature distribution of the plastic hinge for simplification, and consequently obtain the following equations:

$$\phi_u = \frac{\epsilon_{cu}}{x_0} \quad (1)$$

$$\theta_u = Z_p \frac{\epsilon_{cu}}{x_0} \quad (2)$$

$$\Delta = \Delta_u - \Delta_{u1} \quad (3)$$

where Δ denotes the difference in height between the critical section and the anchorage points or deviator points after deformation, namely the vector height shift of external tendons on the critical section after deforma-

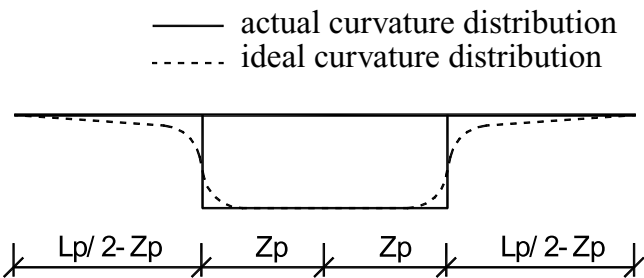


Fig. 19. Curvature distribution of a beam in ultimate bending state.

tion, which closely associates with the so-called second-order effects. The meanings of other notations may be found in the Appendix .

The bending strength of the externally prestressed beam, in view of the influence of second-order effects, can be expressed as

$$M_u = A_s f_y \left(h_0 - \frac{x}{2} \right) + A_p f_{ps} \left(h_p - \frac{x}{2} - \Delta \right) \quad (4)$$

where f_{ps} denotes the final stress in post-tensioned tendons, given by

$$f_{ps} = \sigma_{pe} + \Delta f_{ps} = \sigma_{pe} + \frac{\Delta L_p}{L_p} E_p \quad (5)$$

where Δf_{ps} denotes the stress increment in post-tensioned tendons at ultimate.

The bending strength of externally prestressed beams is associated with a number of factors, including the profile of external tendons, deviator amount and location, effective external prestressing force, geometry of load application, and so on. In particular, this section focuses on the configuration with a double-draped profile and three deviators, just like the one in the test specimen, for a reference to the health monitoring results herein before. This configuration was commonly employed for the distributive load or multiple-point concentrated load, with a critical section generally occurring in the mid-span. Figure 20 illustrates a calculation model for an ultimate bending state of this configuration.

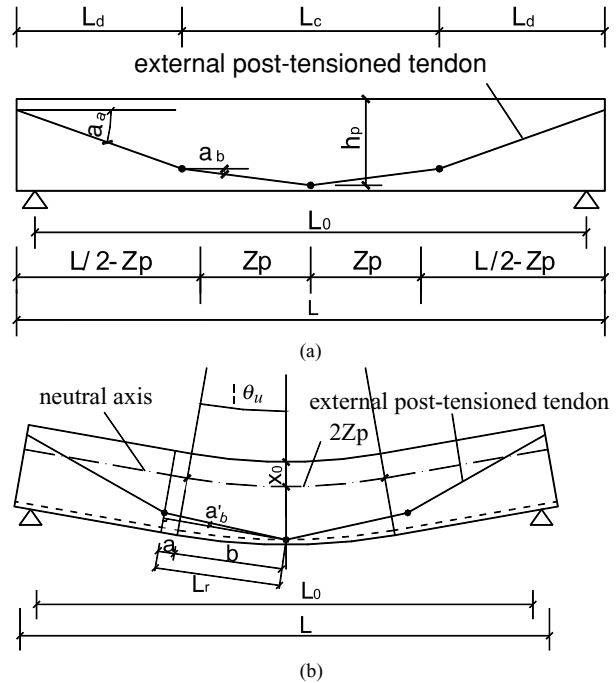


Fig. 20. Calculation model for ultimate bending state: (a) Before deformation; (b) Deformation in ultimate bending state.

According to the calculation model for the ultimate bending state depicted in Figure 20, in which the flexural deformation of the beam was focused only on the portion of plastic hinge existing, Δf_{ps} can also be expressed as

$$\Delta f_{ps} = \frac{\Delta L_p}{L_p} E_p = \frac{\Delta L_p}{L_c / \cos \alpha_b + 2L_d / \cos \alpha_a} E_p \quad (6)$$

where ΔL_p is the elongation of post-tensioned tendon, which is also given by

$$\begin{aligned} \Delta L_p &= L'_p - L_p \\ &= (2L_r / \cos \alpha'_b + 2L_d / \cos \alpha_a) \\ &\quad - (L_c / \cos \alpha_b + 2L_d / \cos \alpha_a) \\ &= 2L_r / \cos \alpha'_b - L_c / \cos \alpha_b \end{aligned} \quad (7)$$

in which L'_p and L_p are the elongated length and the initial length of the post-tensioned tendon, respectively.

As shown in Figure 20b, the following relationship exists for $2L_r$:

$$2L_r = 2(a + b) \quad (8)$$

in which a and b are approximately given by

$$a \approx L_c / 2 - Z_p \quad (9)$$

$$b \approx \left(\frac{Z_p}{\theta_u} + h_p - x_0 \right) \sin \theta_u \quad (10)$$

and thereby obtaining the following equation:

$$2L_r = L_c - 2Z_p + 2 \left(\frac{Z_p}{\theta_u} + h_p - x_0 \right) \sin \theta_u \quad (11)$$

Make a Maclaurin expansion of $\sin \theta_u$, which can be approximately given by

$$\sin \theta_u \approx \theta_u - \frac{\theta_u^3}{6} \quad (12)$$

Consequently, Equation (11) can be expressed as

$$2L_r = 2(h_p - x_0)\theta_u + L_c - \frac{1}{3} Z_p \theta_u^2 \quad (13)$$

According to the geometrical relationship in Figure 20, such an approximation can be obtained:

$$\alpha'_b \approx \alpha_b - \frac{Z_p}{L_c} \theta_u \quad (14)$$

And thus gives:

$$\cos \alpha'_b = \cos \alpha_b \cos \left(\frac{Z_p}{L_c} \theta_u \right) + \sin \alpha_b \sin \left(\frac{Z_p}{L_c} \theta_u \right) \quad (15)$$

And there are also approximations in Equations (16) and (17):

$$\sin \left(\frac{Z_p}{L_c} \theta_u \right) \approx \frac{Z_p}{L_c} \theta_u \quad (16)$$

$$1 - \cos \left(\frac{Z_p \theta_u}{L_c} \right) \approx 2 \sin^2 \left(\frac{Z_p \theta_u}{2L_c} \right) \approx 2 \left(\frac{Z_p \theta_u}{2L_c} \right)^2 = \frac{1}{2} \frac{Z_p^2 \theta_u^2}{L_c^2} \quad (17)$$

Substituting Equations (13), (15), (16), and (17) into Equation (7) gives

$$\begin{aligned} \Delta L_p &= \frac{1}{\cos \alpha'_b} [2(h_p - x_0 - \tan \alpha_b Z_p / 2) \theta_u \\ &\quad - (Z_p / 3 - Z_p^2 / 2L_c) \theta_u^2] \end{aligned} \quad (18)$$

In light of the equilibrium condition of the critical section, namely the section in mid-span, there exists

$$\alpha_1 \beta_1 f_c b x_0 = f_y A_s - f'_y A'_s + (\sigma_{pe} + \Delta f_{ps}) A_p \quad (19)$$

Substituting Equation (18) into Equation (6) gives Δf_{ps} , and then into Equation (19), thus obtains an equation with such a form

$$x_0^3 + Ax_0^2 + Bx_0 + C = 0 \quad (20)$$

in which

$$A = k_2 - k_1 \quad (21)$$

$$B = -k_2 (h_p - \tan \alpha_2 Z_p / 2) \quad (22)$$

$$C = k_2 \varepsilon_{cu} \left(\frac{Z_p}{6} - \frac{Z_p^2}{4L_c} \right) Z_p \quad (23)$$

And for rectangular sections or T-sections with the neutral axis lying in the flange:

$$k_1 = \frac{f_y A_s - f'_y A'_s + \sigma_{pe} A_p}{\alpha_1 \beta_1 f'_c b} \quad (24)$$

For T-sections with a neutral axis lying in the web:

$$k_1 = \frac{f_y A_s - f'_y A'_s + \sigma_{pe} A_p - \alpha_1 \beta_1 f'_c (b_f - b) h_f}{\alpha_1 \beta_1 f'_c b} \quad (25)$$

Although for all these three types of sections

$$k_2 = \frac{2E_p A_p Z_p \varepsilon_{cu}}{\alpha_1 \beta_1 f'_c b (L_c + 2L_d \cos \alpha_b / \cos \alpha_a)} \quad (26)$$

Solve Equation (20) and chose a proper root x_0 from all the three ones, and then obtain the parameter x in Equation (4), which is the actual height of the compressive region, given by

$$x = \beta_1 x_0 \quad (27)$$

Substituting Equation (18) into Equation (5) and then into Equation (4), together with Equation (3) and Equation (27), finally achieve the ultimate bending moment M_u .

However, what has to be mentioned is that for the configuration of the test specimen, Δ is just equal to zero owing to the same height of the three deviators.

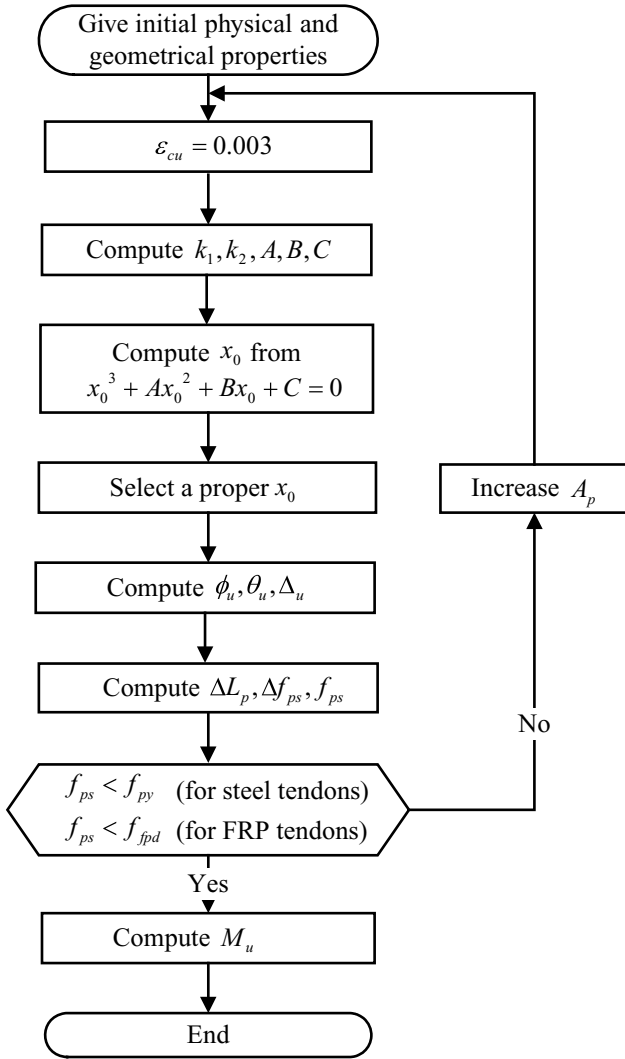


Fig. 21. Flowchart of computational procedure.

6.2 Computational procedure

A computational program was developed based on the model herein above, and the flowchart is shown as Figure 21.

Table 2 presents a comparison of the theoretical and experimental ultimate values, where the letter T denotes theoretical values, and S1 and S2 denote experimental values of S1 and S2, respectively. The result is very satisfactory because the theoretical values are all very much close to the experimental ones.

6.3 Identification of alert values

Adopt the maximal compressive strain of concrete ε_{cm} and the maximal tensile strain of AFRP tendon ε_{pm} as two major alert parameters for structural state evaluation. The relevant alert values $[\varepsilon_{cm}]$ and $[\varepsilon_{pm}]$ can be

Table 2

Comparison of experimental and theoretical ultimate values

	M_u (kNm)	ε_{cu} ($\mu\varepsilon$)	ε_{ps} ($\mu\varepsilon$)
T	86	3,000	16,318
S1	88	3,050	15,820
S2	88	3,170	16,640

Table 3

Evaluation of structural health state using different safety factors ($\mu\varepsilon$)

Safety factor	Ultimate values		Alert values		Test values		Evaluation
	ε_{cu}	ε_{ps}	$[\varepsilon_{cm}]$	$[\varepsilon_{pm}]$	ε_{cm}	ε_{pm}	
1.2			2,500	13,598			Safety
1.5	3,000	16,318	2,000	10,879	421	9,105	Safety
2			1,500	8,159			Alarm

obtained directly via dividing a safety factor to the theoretical ultimate values. And the value of the safety factor will be determined by the bridge administrators via a tradeoff between importance and budget. For instance, given a set of safety factor values like 1.2, 1.5, and 2, that is to say, respectively, 16.7%, 33.3%, and 50% of total bending strength is to be held for safety reservation. Table 3 demonstrates the structural state evaluation process of the test specimen, by comparing the test values from the HMS with their respective alert values. Only for the case with a safety factor of 2, the test value ε_{pm} exceeds its alert value, and therefore an alarm should be sent. A conclusion of structural safety can be reached for the other two cases.

7 SUMMARY AND CONCLUSIONS

The investigation presented in this article focuses on two relevant aspects concerning structural health monitoring and evaluation. On the one hand, two types of DOFS, namely FBG and BOTDR, were employed into an integrated HMS for rehabilitated RC girder bridges by means of a series of static and dynamic loading tests to a simply supported RC T-beam strengthened by externally post-tensioned AFRP tendons. On the other hand, based on the bending strength of externally prestressed members, ultimate values for the test specimen were numerically computed via a newly developed simplified model. And by adopting safety factors, relevant alert values were obtained to compare with the monitoring results to give a structural state evaluation of the beam.

Results of calibration tests, respectively, for FBG and BOTDR before the loading tests were implemented to obtain good linear behavior for both of them. And the real-time monitoring results also well identified the relevant structural state for each loading stage. Therefore, the newly developed HMS integrated both DOFS systems and was proved to be of great efficiency for operation, and consequently holds a great potential for the rehabilitated concrete bridges strengthened by external prestressing.

With regard to methodologies for the structural state evaluation of rehabilitated concrete bridges, the model developed in this article satisfactorily predicted the structural performance of the test beam at ultimate no matter whether or not fatigue exists. However, further investigation of the model still needs to be performed in view of more detailed factors, such as rigidity degradation under fatigue and full-range nonlinear analysis for a more general prediction.

ACKNOWLEDGMENTS

The research was financially supported by the National Science Fund for Distinguished Young Scholars of China with the grant number of 40225006, and the key project of Educational Ministry of China with the grant number of 01086.

REFERENCES

- Aktan, A. E., Catbas, F. N., Grimmelsman, K. A. & Tsikos, C. J. (2000), Issues in infrastructure health monitoring for management, *Journal of Engineering Mechanics-ASCE*, **126**(7), 711–24.
- Aktan, A. E., Helmicki, A. J. & Hunt, V. J. (1998), Issues in health monitoring for intelligent infrastructure, *Smart Materials and Structures*, **7**(5), 674–92.
- Ansari, F. (1997), State-of-the-art in the applications of fiber-optic sensors to cementitious composites, *Cement & Concrete Composites*, **19**(1), 3–19.
- Bao, X. Y., Demerchant, M., Brown, A. & Bremner, T. (2001), Tensile and compressive strain measurement in the lab and field with the distributed Brillouin scattering sensor, *Journal of Lightwave Technology*, **19**(10), 1698–704.
- Casas, J. R. & Ramos, G. (2002), Intelligent repair of existing concrete structures, *Computer-Aided Civil and Infrastructure Engineering*, **17**(1), 43–52.
- Davis, M. A., Bellemore, D. G. & Kersey, A. D. (1997), Distributed fiber Bragg grating strain sensing in reinforced concrete structural components, *Cement & Concrete Composites*, **19**(1), 45–57.
- Harajli, M., Khairallah, N. & Nassif, H. (1999), Externally prestressed members: Evaluation of second-order effects, *Journal of Structural Engineering-ASCE*, **125**(10), 1151–61.
- Hiroshige, O., Hiroshi, N., Mitsuru, K. & Akiyoshi, S. (2001), Industrial applications of the BOTDR optical fiber strain sensor, *Optical Fiber Technology*, **7**(1), 45–64.
- Komatsu, K., Fujihashi, K. & Okutsu, M. (2002), Application of the optical sensing technology to the civil engineering field with optical fiber strain measurement device (BOTDR), *Proceedings of SPIE*, 4920, 352–61.
- Kurashima, T., Usu, T., Tanaka, K. & Nobiki, A. (1997), Application of fiber optic distributed sensor for strain measurement in civil engineering, *Proceedings of SPIE*, 3241, 247–58.
- Lin, Y. B., Chang, K. C., Chern, J. C. & Wang, L. A. (2004), The health monitoring of a prestressed concrete beam by using fiber Bragg grating sensors, *Smart Materials and Structures*, **13**(4), 712–18.
- Maaskant, R., Alavie, T., Measures, R. M., Tadros, G., Rizkalla, S. H. & Guha-Thakurta, A. (1997), Fiber-optic Bragg grating sensors for bridge monitoring, *Cement & Concrete Composites*, **19**(1), 21–33.
- Naaman, A. E. (1995), Unified bending strength design of concrete members: AASHTO LRFD Code, *Journal of Structural Engineering-ASCE*, **121**(6), 964–70.
- Tan, K. H. & Ng, C. K. (1997), Effects of deviators and tendon configuration on behavior of externally prestressed beams, *ACI Structural Journal*, **94**(1), 13–22.
- Wu, Z. S., Xu, B., Hayashi, K. & Machida, A. (2003), Fiber optic sensing of PC girder strengthened with prestressed PBO fiber sheets, in Z. S. Wu & M. Abe (eds.), *Proceedings of the First International Conference on Structural Health Monitoring and Intelligent Infrastructures*, Tokyo, 13–15 November 2003, Rotterdam, Balkema.

APPENDIX: NOTATION

The following symbols are used in this article:

- M_u : nominal moment resistance at ultimate;
 A_p : area of prestressing tendon in tension zone;
 A_s : area of nonprestressed tension steel;
 A'_s : area of nonprestressed compression steel;
 f_y : specified yield strength of tensile reinforcement;
 f'_y : specified yield strength of compressive reinforcement;
 f_{ps} : stress in prestressing tendon at ultimate;
 Δf_{ps} : stress increment in prestressing tendon at ultimate;
 σ_{pe} : effective stress in prestressing tendon, after prestress loss, at section considered;
 h_0 : distance from extreme compression fiber to centroid of nonprestressed tension reinforcement;
 h_p : distance from extreme compression fiber to centroid of external prestressing tendon reinforcement;
 x : actual height of compressive region;
 x_0 : equivalent height of compressive region;
 Δ : vector height shift of external tendon on critical section after deformation;
 Δ_u : deflection in mid-span;
 Δ_{u1} : deflection of outer deviator;
 L_p : initial length of tendon;
 L'_p : elongated length of tendon;
 ΔL_p : elongation of the post-tensioned tendon;

E_p : modulus of elasticity of pre-stressing tendon;
 ϵ_{cu} : assumed concrete strain in extreme compression
 fiber at nominal resistance (=0.003 by ACI);
 ϕ_u : curvature in plastic hinge zone;
 θ_u : a half of total rotation in plastic hinge zone;
 Z_p : length of plastic hinge zone, given by:

$$Z_p = \begin{cases} 0.5d_e + 0.05Z & \text{single-point} \\ & \text{loading} \\ 0.5(L_0 + d_e) & \text{with a uniform} \\ & \text{bending region;} \end{cases}$$

L : component length;
 L_0 : span length;
 L_m : length of uniform bending region;
 L_d : distance between anchorage and its nearest
 deviator;
 L_c : distance between the two outer deviators;

L_r : length between the middle deviator and an outer
 deviator after deformation;
 a : length between the outer deviator and near limit
 of uniform bending region after deformation;
 b : length between the middle deviator and limit of
 uniform bending region after deformation;
 α_a : slope angle of the outer section of pre-stressing
 tendon;
 α_b : slope angle of the inner section of pre-stressing
 tendon before deformation
 α_1 : ratio of the average concrete stress to concrete
 strength;
 β_1 : factor used to define depth of equivalent rectan-
 gular stress block at ultimate as a function of the
 neutral axis location;
 f_{py} : specified yield strength of external pre-stressing
 steel; and
 f_{fpd} : specified yield strength of external pre-stressing
 FRP tendon.